Sensorless Control of Standalone Brushless Doubly Fed Induction Generator Feeding Unbalanced Loads in a Ship Shaft Power Generation System

Liu, Yi; Xu, Wei; Zhu, Jianguo; Blaabjerg, Frede

Published in:
I E E E Transactions on Industrial Electronics

DOI (link to publication from Publisher):
10.1109/TIE.2018.2835400

Publication date:
2019

Document Version
Accepted author manuscript, peer reviewed version

This article has been accepted for publication in a future issue of this journal, but has not been fully edited. Content may change prior to final publication. Citation information: DOI 10.1109/TIE.2018.2835400, IEEE Transactions on Industrial Electronics

Sensorless Control of Standalone Brushless Doubly-Fed Induction Generator Feeding Unbalanced Loads in Ship Shaft Power Generation System

Yi Liu, *Member*, *IEEE*, Wei Xu, *Senior Member*, *IEEE*, Jianguo Zhu, *Senior Member*, *IEEE*, and Frede Blaabjerg, *Fellow*, *IEEE*

***Abstract*—The standalone brushless doubly-fed induction generator (BDFIG) has demonstrated excellent energy saving performance in ship shaft power generation applications. As a standalone system, it exhibits unbalanced terminal voltages and poor performance under unbalanced loads. However, the existing control scheme of grid-connected BDFIGs cannot be directly applied to stabilize the amplitude and frequency of terminal voltage when the rotor speed and electrical load vary. This paper presents a new sensorless control scheme for the standalone BDFIG under unbalanced load conditions in the ship shaft power generation system. A second-order generalized integrator based quadrature signal generator is introduced to realize the rotor speed observer for the standalone BDFIG feeding unbalanced loads. The compensation method of negative-sequence power winding voltage is proposed to eliminate the negative-sequence component of the unbalanced power winding voltage. Comprehensive experiments are carried out on a prototype BDFIG with and without the compensation of negative-sequence power winding voltage. The good performance of the proposed sensorless control scheme is verified by the experimental test results.**

***Index Terms*—Brushless doubly-fed induction generator (BDFIG), unbalanced load, sensorless control, ship shaft power generation, standalone operation.**

Manuscript received November 3, 2017; revised February 7, 2018 and April 6, 2018; accepted May 1, 2018. This work was supported in part by the National Natural Science Foundation of China under Grant 51707079, and in part by China Postdoctoral Science Foundation under Grant 2017M622443.

Y. Liu and W. Xu are with the State Key Laboratory of Advanced Electromagnetic Engineering and Technology, School of Electrical and Electronic Engineering, Huazhong University of Science and Technology, Wuhan, 430074, China (e-mail: liuyi82@hust.edu.cn; weixu@hust.edu.cn).

J. Zhu is with the School of Electrical and Information Engineering, University of Sydney, Sydney, Australia (e-mail: jianguo.zhu@sydney.edu.au).

F. Blaabjerg is with the Department of Energy Technology, Aalborg University, Aalborg DK-9220, Denmark (e-mail: fbl@et.aau.dk).

Corresponding author: Wei Xu (phone: 0086-027-87558623; fax: 0086-027-89540937; email: weixu@hust.edu.cn).

NOMENCLATURE

p_1, p_2	Pole pair numbers of power winding (PW) and control winding (CW).
ω_1, ω_2	Angular frequencies of PW and CW.
ω_r, ω_N	Actual and natural synchronous rotor speeds.
θ_1, θ_2	Angular positions of PW voltage and CW current vectors.
θ_{rv}	Virtual rotor position.
P_1, P_2, P_{out}	Active powers of PW and CW, and output active power of the standalone BDFIG.
$\boldsymbol{U}$, $\boldsymbol{I}$, $\boldsymbol{\Psi}$	Voltage, current, and flux vectors.
u, i, ψ	Voltage, current, and flux scalars.
R_1, R_2, R_r	Resistances of PW, CW, and rotor.
L_1, L_2, L_r	Self-inductances of PW, CW, and rotor.
L_{1r}, L_{2r}	Coupling inductances between the stator and rotor windings.
s	Differential operator, i.e., d/dt.

Superscripts

+, -	Variables of the positive- and negative-sequence PW voltage controllers.
*	Reference value.
^	Estimated value.

Subscripts

1, 2, r	PW, CW, and rotor.
d, q	Synchronous rotating dq axes.
α, β	Stationary $\alpha\beta$ axes.
f	Filtered quantity.
ff	Feedforward quantity.
S	Steady-state value.

I. INTRODUCTION

THE brushless doubly-fed induction generator (BDFIG) consists of a specially designed rotor and two sets of stator windings with different number of pole pairs, in which the indirect electromagnetic coupling effect between the two stator windings is generated via the rotor [1], [2]. Compared with the conventional wound rotor doubly-fed induction generator (DFIG), the BDFIG, without electric brushes and slip rings, has

This article has been accepted for publication in a future issue of this journal, but has not been fully edited. Content may change prior to final publication. Citation information: DOI 10.1109/TIE.2018.2835400, IEEE Transactions on Industrial Electronics

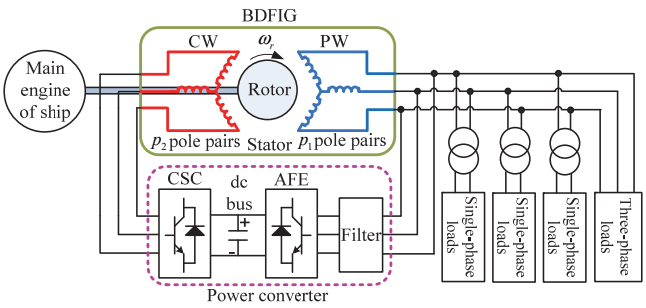

Fig. 1. Structure of the standalone BDFIG system for ship shaft power generation applications, where PW stands for power winding, CW for control winding, CSC for CW side converter, and AFE for active front end.

the merits of longer work lifetime, higher reliability and lower maintenance cost [3].

The standalone BDFIG has exhibited excellent energy saving performance in variable speed constant frequency ship shaft power generation systems. It can be connected to the main engine of the ship directly or through a gearbox to exploit the redundant power of the main engine for power generation by employing a fractionally rated power converter [4]. The structure of the standalone BDFIG system for ship shaft power generation applications is shown in Fig. 1, where the CW is supplied by a CW side converter with the frequency variable exciting current, and an active front end rectifier with a filter is connected to the PW to regulate the dc bus voltage and to achieve the bidirectional power flow. Generally, the electrical loads of a ship include both three-phase loads and single-phase loads. If the three-phase loads fail, or the loads on the three single-phase power lines are unequal, the total three-phase load of the power generation system would be unbalanced. The unbalanced load would cause unbalanced three-phase PW current, and result in unbalanced three-phase PW terminal voltage.

The vector control schemes of the grid-connected BDFIG wind power generation system under balanced and unbalanced grid conditions have been proposed in [5]-[7] with the active and reactive power as the control objectives. Unlike the grid-connected BDFIG, the standalone BDFIG system should stabilize the amplitude and frequency of the output voltage when the rotor speed and electrical load vary. Hence, the control scheme of the grid-connected BDFIG cannot be directly applied to the standalone BDFIG.

For a standalone BDFIG feeding balanced three-phase loads, a direct voltage control scheme for standalone wind energy conversion systems has been developed in [8]. The transient control of reactive current for the active front end rectifier in the standalone BDFIG power generation system has been proposed to improve the quality of output voltage [9]. Without considering the unbalanced loads, a control scheme for the standalone BDFIG ship shaft power generation system has been designed [10] and analyzed [11], based on the CW current orientation. However, no study has been reported on the control scheme for standalone BDFIGs feeding unbalanced loads.

Many other typical BDFIG control schemes have also been proposed, such as the fault ride-through control [12], generalized vector control [13], phase angle control [14], indirect stator-quantities control [15], and direct torque control [16].

It should be noted that all the control schemes proposed in [5]-[10] and [12]-[16] have employed mechanical sensors to acquire the information of rotor position/speed. In [5], [6], [8], [10] and [12]-[13], the measured rotor positions are employed to calculate the reference angles for the *dq* transformation of the CW voltage and current. In addition, in [7], the rotor speed is required to derive the feedforward component for obtaining the CW current reference. In [9], a scalar control scheme is employed in the machine side converter of BDFIG, in which the rotor speed is measured in order to calculate the reference frequency of CW. In [10], the CW frequency, serving as the feedforward component of the PW frequency controller, is derived from the measured rotor speed. The control schemes proposed in [13]-[15] deal with the speed control of BDFIG, in which the measured rotor speeds serve as the rotor speed feedback. Specially, the measured rotor speed in [16] is utilized to estimate the CW flux and the BDFIG electromagnetic torque. However, the use of a rotor position/speed sensor brings many drawbacks, such as higher cost, more system complexity, less reliability, and limited installation flexibility.

In [17], a decoupling network method for inner current loops of standalone BDFIG systems has been designed without using the rotor position information. However, it was admitted that the sensorless direct voltage control scheme and the decoupling network method could not run well under unbalanced load conditions. The rotor speed observer (RSO) based on the PW flux estimation for the brushless doubly-fed reluctance generator has been developed in [18] and [19], which needs the information of the PW inductance and resistance. However, in the standalone BDFIG system, the unbalanced load would cause unbalanced PW voltage and current, consequently generating distorted PW flux. As a result, the rotor speed estimated by the RSO would be inaccurate due to the distorted PW flux, and the robustness of the RSO limited due to the dependence on BDFIG parameters.

For sensorless operation of the standalone BDFIG feeding unbalanced loads, this paper proposes a new RSO, which is independent of machine parameters except the number of pole pairs. Based on the proposed RSO, a sensorless control scheme is then developed. The effectiveness of the proposed RSO and sensorless control scheme is validated by experimental test results.

II. Operation Principle and Dynamic Vector Model of BDFIG

A. Basic Operation Principle

The BDFIG can be operated in various modes, including the doubly-fed, cascaded, and induction modes [3]. Among them, the doubly-fed mode is the optimal one, in which the rotor speed can be expressed as

$$\omega_r = (\omega_1 + \omega_2)/(p_1 + p_2) \tag{1}$$

When ω_2 is zero, the rotor is rotating at the natural synchronous speed ω_N. The rotor speed above ω_N is called the

This article has been accepted for publication in a future issue of this journal, but has not been fully edited. Content may change prior to final publication. Citation information: DOI 10.1109/TIE.2018.2835400, IEEE Transactions on Industrial Electronics

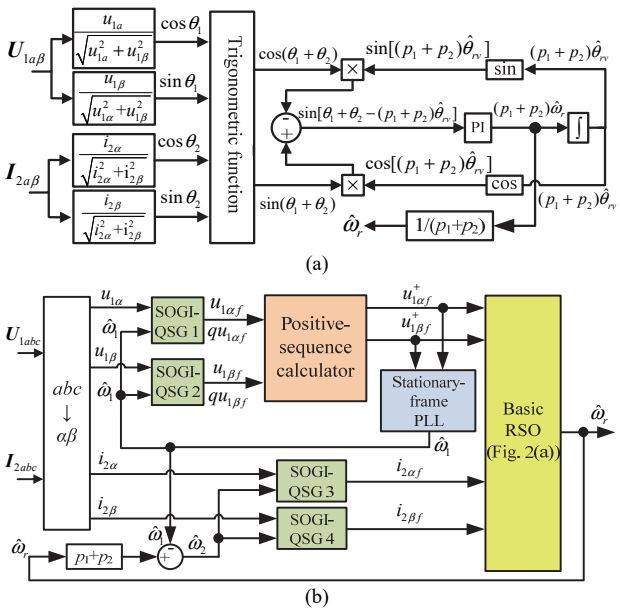

Fig. 2. Structures of (a) Basic, and (b) Improved rotor speed observers (RSOs).

super-synchronous speed, and that below ω_N the sub-synchronous speed. When the rotor speed varies, in order to maintain constant PW frequency ω_1, ω_2 should be changed by

$$\omega_2 = \omega_r(p_1 + p_2) - \omega_1 . \tag{2}$$

When ignoring the loss of the power converters, the output active power of the standalone BDFIG, P_{out}, is the sum of the active powers of the PW and CW, P_1 and P_2, i.e.

$$P_{out} = P_1 + P_2 . \tag{3}$$

Consequently, the PW active power can be expressed in relation to the rotor speed as follows [11]:

$$P_1 = \omega_1 P_{out} / [\omega_r(p_1 + p_2)] . \tag{4}$$

From (4), it can be seen that the PW active power will be reduced when the rotor speed increases under constant load.

B. Dynamic Vector Modelling

The unified reference frame dq vector model is employed in this paper and it is expressed as [20]:

$$\begin{cases} \boldsymbol{U}_{1dq} = R_1 \boldsymbol{I}_{1dq} + s\boldsymbol{\Psi}_{1dq} + j\omega_a \boldsymbol{\Psi}_{1dq} \\ \boldsymbol{\Psi}_{1dq} = L_1 \boldsymbol{I}_{1dq} + L_{1r} \boldsymbol{I}_{rdq} \\ \boldsymbol{U}_{2dq} = R_2 \boldsymbol{I}_{2dq} + s\boldsymbol{\Psi}_{2dq} + j[\omega_a - (p_1 + p_2)\omega_r] \boldsymbol{\Psi}_{2dq} \\ \boldsymbol{\Psi}_{2dq} = L_2 \boldsymbol{I}_{2dq} + L_{2r} \boldsymbol{I}_{rdq} \\ \boldsymbol{U}_{rdq} = R_r \boldsymbol{I}_{rdq} + s\boldsymbol{\Psi}_{rdq} + j(\omega_a - p_1\omega_r) \boldsymbol{\Psi}_{rdq} \\ \boldsymbol{\Psi}_{rdq} = L_r \boldsymbol{I}_{rdq} + L_{1r} \boldsymbol{I}_{1dq} + L_{2r} \boldsymbol{I}_{2dq} \end{cases} \tag{5}$$

where ω_a is the angular frequency of the rotating dq reference frame.

III. Design of Rotor Speed Observer

The proposed control scheme just requires the accurate rotor speed information, but not necessarily the real rotor position. When ignoring the integration constant, the following relationship can be derived for the rotor position by integrating both sides of (1):

$$(p_1 + p_2)\theta_{rv} = \theta_1 + \theta_2 \tag{6}$$

where θ_{rv} is the virtual rotor position, which is not the accurate rotor position by the general definition.

Therefore, from (6), the difference between the actual and estimated virtual rotor positions, $\Delta\theta_{rv}$, can be derived as

$$\begin{aligned} (p_1 + p_2)\Delta\theta_{rv} &= (p_1 + p_2)(\theta_{rv} - \hat{\theta}_{rv}) \\ &= (\theta_1 + \theta_2) - (p_1 + p_2)\hat{\theta}_{rv} \end{aligned} . \tag{7}$$

When the system is working in the quasi-locked state (i.e., $\omega_r = \hat{\omega}_r$, $\theta_r \approx \hat{\theta}_{rv}$), the value of (7) will be sufficiently small, and $(p_1+p_2)\Delta\theta_{rv}$ can be approximated as $\sin[(\theta_1 + \theta_2) - (p_1 + p_2)\hat{\theta}_{rv}]$. Hence, based on the principle of the stationary-frame phase-locked loop (PLL) [21], the basic RSO as shown in Fig. 2(a) can be employed to obtain the rotor speed [22], in which the virtual rotor position θ_{rv} is just an intermediate variable.

In the standalone BDFIG system, since the PW voltage is generated by injecting an exciting current in the CW, the CW current is never zero even under the no-load condition [17]. In addition, once the CW current is not zero, the PW voltage will be generated. So, there can be no case of the zero voltage of the PW side and zero current of the CW side. Consequently, $\sin\theta_1$ and $\cos\theta_1$ can be obtained from the three-phase PW voltage, and $\sin\theta_2$ and $\cos\theta_2$ from the three-phase CW current, as shown in Fig. 2(a). Hence, the basic RSO can observe the rotor speed of the standalone BDFIG based on the three-phase PW voltage and the three-phase CW current. The parameter tuning method of the PI controller in Fig. 2(a) can refer to [22].

However, an unbalanced load would result in an unbalanced three-phase PW current, which could produce different voltage drops across the three-phase PW impedances, resulting in unbalanced PW terminal voltages. The negative-sequence PW current would induce abundant harmonic current in the CW due to the indirect coupling between the PW and CW via the rotor. When using the basic RSO, the rotor speed cannot be accurately estimated by the unbalanced PW voltage and distorted CW current.

To solve this problem, the second-order generalized integrator-based quadrature-signal generator (SOGI-QSG) [23] and the positive-sequence calculator [6] are introduced to construct the improved RSO for the standalone BDFIG under unbalanced load conditions, as shown in Fig. 2(b). The SOGI-QSGs 1 and 2 is used to obtain the filtered results ($u_{1\alpha f}$ and $u_{1\beta f}$) and 90° phase-shifted versions ($qu_{1\alpha f}$ and $qu_{1\beta f}$) of the α- and β-components of the PW voltage. The α- and β-components of the positive-sequence PW voltage, $u^+_{1\alpha f}$, $u^+_{1\beta f}$, are derived from the positive-sequence calculator and sent to the stationary-frame PLL to make the SOGI-QSGs 1 and 2 frequency-adaptive. The SOGI-QSGs 3 and 4 are employed to filter the α- and β-components of the CW current, where the resonance frequency is derived from (2). Finally, these quantities $u^+_{1\alpha f}$, $u^+_{1\beta f}$, $i_{2\alpha f}$ and $i_{2\beta f}$ are input to the basic

This article has been accepted for publication in a future issue of this journal, but has not been fully edited. Content may change prior to final publication. Citation information: DOI 10.1109/TIE.2018.2835400, IEEE Transactions on Industrial Electronics

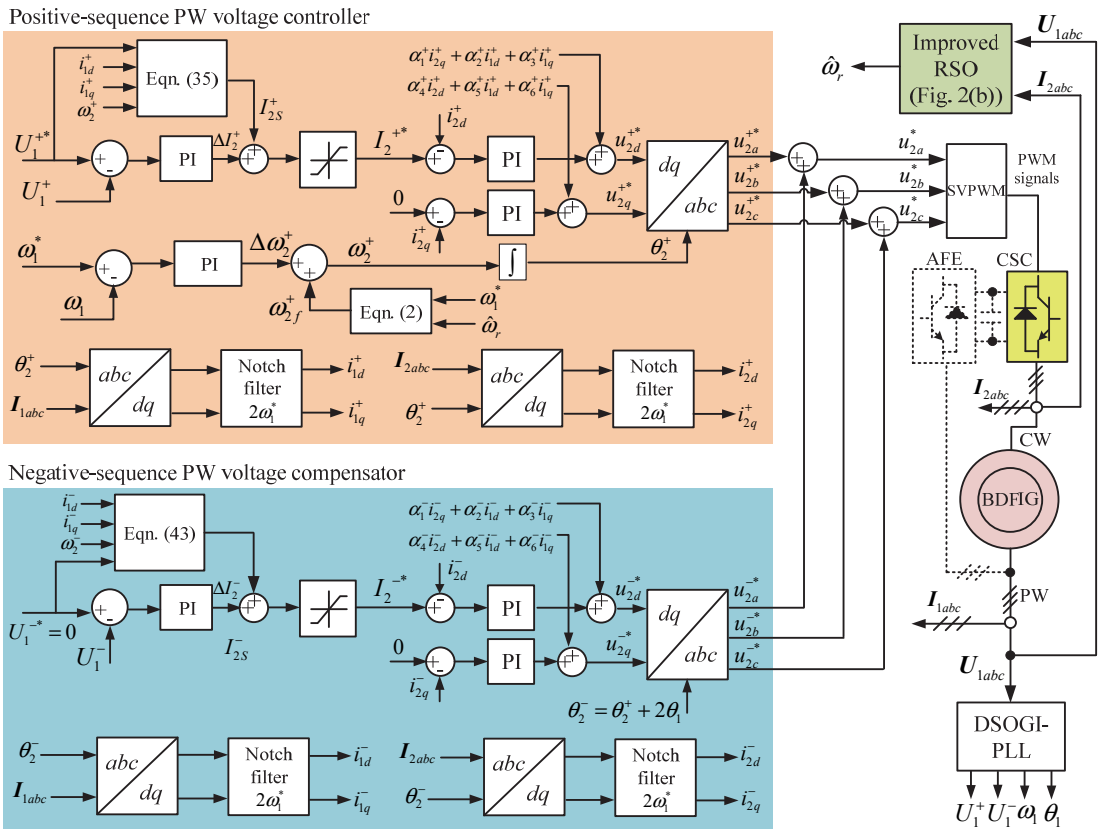

Fig. 3. Overall sensorless control scheme of the standalone BDFIG feeding unbalanced loads.

RSO to obtain the accurate rotor speed.

IV. Control Scheme Development

A. Overall Sensorless Control Scheme

According to the instantaneous symmetrical component method, the unbalanced three-phase voltage can be decomposed to balanced positive-, negative- and zero-sequence components. In a ship shaft power generation system, the BDFIG is connected to the loads through the three-phase three-wire system, which has no neutral line, or the path for the zero-sequence current components. Hence, only the negative-sequence component of the output voltage need to be compensated in the proposed control scheme.

The overall sensorless control scheme, as shown in Fig. 3, consists of the positive-sequence PW voltage controller, the negative-sequence PW voltage compensator, the improved RSO, and the dual second-order generalized integrator PLL (DSOGI-PLL). The improved RSO is employed to estimate the rotor speed, which would be used in the control of the PW frequency and the calculation of the feed-forward compensation in the current loops of the positive-sequence PW voltage controller and the negative-sequence PW voltage compensator.

The DSOGI-PLL can be employed to estimate the amplitudes, frequencies and phase angles of the positive- and negative-sequence PW voltages, which is with good steady-state and dynamic performance when the three-phase voltages contain unbalanced drops [23].

B. Positive-Sequence PW Voltage Controller

According to (2), in order to generate the positive-sequence PW voltage, the CW current frequency in the positive-sequence PW voltage controller, ω_2^+, should be specified by

$$\omega_2^+ = \omega_r(p_1 + p_2) - \omega_1 . \tag{8}$$

The proposed positive-sequence PW voltage controller is based on the CW current vector orientation, i.e. substituting ω_a in (5) with ω_2^+, and the dynamic model of the BDFIG can be rewritten as

$$\begin{cases} \boldsymbol{U}_{1dq}^+ = R_1\boldsymbol{I}_{1dq}^+ + s\boldsymbol{\Psi}_{1dq}^+ + j\omega_2^+\boldsymbol{\Psi}_{1dq}^+ \\ \boldsymbol{\Psi}_{1dq}^+ = L_1\boldsymbol{I}_{1dq}^+ + L_{1r}\boldsymbol{I}_{rdq}^+ \\ \boldsymbol{U}_{2dq}^+ = R_2\boldsymbol{I}_{2dq}^+ + s\boldsymbol{\Psi}_{2dq}^+ + j[\omega_2^+ - (p_1+p_2)\omega_r]\boldsymbol{\Psi}_{2dq}^+ \\ \boldsymbol{\Psi}_{2dq}^+ = L_2\boldsymbol{I}_{2dq}^+ + L_{2r}\boldsymbol{I}_{rdq}^+ \\ \boldsymbol{U}_{rdq}^+ = R_r\boldsymbol{I}_{rdq}^+ + s\boldsymbol{\Psi}_{rdq}^+ + j(\omega_2^+ - p_1\omega_r)\boldsymbol{\Psi}_{rdq}^+ \\ \boldsymbol{\Psi}_{rdq}^+ = L_r\boldsymbol{I}_{rdq}^+ + L_{1r}\boldsymbol{I}_{1dq}^+ + L_{2r}\boldsymbol{I}_{2dq}^+ \end{cases} . \tag{9}$$

Rearranging (8), one obtains $\omega_2^+ - p_1\omega_r = -(\omega_1 - p_2\omega_r)$. By substituting this equation into the 5th equation of (9) and setting the rotor voltage to zero, the 5th and 6th equations of (9) in the form of d- and q-components can be expressed as

$$u_{rd}^+ = 0 = R_r i_{rd}^+ + s\psi_{rd}^+ + (\omega_1 - p_2\omega_r)\psi_{rq}^+ \tag{10}$$

$$u_{rq}^+ = 0 = R_r i_{rq}^+ + s\psi_{rq}^+ - (\omega_1 - p_2\omega_r)\psi_{rd}^+ \tag{11}$$

$$\psi_{rd}^+ = L_r i_{rd}^+ + L_{1r} i_{1d}^+ + L_{2r} i_{2d}^+ \tag{12}$$

$$\psi_{rq}^+ = L_r i_{rq}^+ + L_{1r} i_{1q}^+ + L_{2r} i_{2q}^+ . \tag{13}$$

This article has been accepted for publication in a future issue of this journal, but has not been fully edited. Content may change prior to final publication. Citation information: DOI 10.1109/TIE.2018.2835400, IEEE Transactions on Industrial Electronics

Substituting (12) and (13) into (10) and (11) yields

$$i_{rd}^{+}=-\frac{[L_r s^2+R_r s+L_r(\omega_1-p_2\omega_r)^2](L_{1r}i_{1d}^{+}+L_{2r}i_{2d}^{+})}{(R_r+L_r s)^2+L_r^2(\omega_1-p_2\omega_r)^2}-\frac{R_r(\omega_1-p_2\omega_r)(L_{1r}i_{1q}^{+}+L_{2r}i_{2q}^{+})}{(R_r+L_r s)^2+L_r^2(\omega_1-p_2\omega_r)^2} \quad (14)$$

$$i_{rq}^{+}=\frac{\omega_1-p_2\omega_r}{R_r+L_r s}\left[1-\frac{L_r^2 s^2+L_r R_r s+L_r^2(\omega_1-p_2\omega_r)^2}{(R_r+L_r s)^2+L_r^2(\omega_1-p_2\omega_r)^2}\right]*(L_{1r}i_{1d}^{+}+L_{2r}i_{2d}^{+})-\frac{1}{R_r+L_r s}(L_{1r}i_{1q}^{+}+L_{2r}i_{2q}^{+})*\left[s+\frac{L_r R_r(\omega_1-p_2\omega_r)^2}{(R_r+L_r s)^2+L_r^2(\omega_1-p_2\omega_r)^2}\right] \quad . \quad (15)$$

In order to employ a fractionally rated power converter to drive the standalone BDFIG system, the CW angular frequency ω_2 is usually limited to 30% of the PW frequency, and thus the rotor speed range is limited according to (1). Consequently, the value of $(\omega_1-p_2\omega_r)^2$ will be much greater than 1. Since in general the values of R_r and L_r are close, R_r^2 is much smaller than $L_r^2(\omega_1-p_2\omega_r)^2$, and R_r^2 in the denominator of the first term of (14) can be ignored. Therefore, the first term of (14) can be approximately written as

$$-\frac{[s^2+(R_r/L_r)s+(\omega_1-p_2\omega_r)^2](L_{1r}i_{1d}^{+}+L_{2r}i_{2d}^{+})}{L_r[s^2+2(R_r/L_r)s+(\omega_1-p_2\omega_r)^2]}.$$

Since the zeros and poles of this term are very close such that they can cancel each other, the first term of (14) can be simplified as $-(L_{1r}i_{1d}^{+}+L_{2r}i_{2d}^{+})/L_r$.

In the steady state, the $(R_r+L_r s)^2$ in the denominator of the second term of (14) would be much smaller than $L_r^2(\omega_1-p_2\omega_r)^2$ and can be ignored. Consequently, the second term in (14) can be simplified as

$$-\left[R_r(L_{1r}i_{1q}^{+}+L_{2r}i_{2q}^{+})\right]/\left[L_r^2(\omega_1-p_2\omega_r)\right].$$

Therefore, (14) can be simplified as

$$i_{rd}=-\frac{L_{1r}i_{1d}^{+}+L_{2r}i_{2d}^{+}}{L_r}-\frac{R_r(L_{1r}i_{1q}^{+}+L_{2r}i_{2q}^{+})}{L_r^2(\omega_1-p_2\omega_r)}. \quad (16)$$

Similarly, (15) can be simplified as

$$i_{rq}^{+}=-(L_{1r}i_{1q}^{+}+L_{2r}i_{2q}^{+})/L_r. \quad (17)$$

Since $\omega_2^{+}-(p_1+p_2)\omega_r=-\omega_1$, splitting the 3rd and 4th equations of (9) into the *d*- and *q*-components results in

$$u_{2d}^{+}=R_2 i_{2d}^{+}+s\psi_{2d}^{+}+\omega_1\psi_{2q}^{+} \quad (18)$$

$$u_{2q}^{+}=R_2 i_{2q}^{+}+s\psi_{2q}^{+}-\omega_1\psi_{2d}^{+} \quad (19)$$

$$\psi_{2d}^{+}=L_2 i_{2d}^{+}+L_{2r}i_{rd}^{+} \quad (20)$$

$$\psi_{2q}^{+}=L_2 i_{2q}^{+}+L_{2r}i_{rq}^{+}. \quad (21)$$

Substituting (16) and (17) in (18)-(21) yields

$$u_{2d}^{+}=K_{2d}^{+}i_{2d}^{+}+D_{2d}^{+} \quad (22)$$

$$u_{2q}^{+}=K_{2q}^{+}i_{2q}^{+}+D_{2q}^{+} \quad (23)$$

where $K_{2d}^{+}=K_{2q}^{+}=R_2+\sigma_2 L_2 s$, $D_{2d}^{+}=\alpha_1^{+}i_{2q}^{+}+\alpha_2^{+}i_{1d}^{+}+\alpha_3^{+}i_{1q}^{+}$, $D_{2q}^{+}=\alpha_4^{+}i_{2d}^{+}+\alpha_5^{+}i_{1d}^{+}+\alpha_6^{+}i_{1q}^{+}$, and $\sigma_2=1-L_{2r}^2/(L_2L_r)$ is the leakage constant of CW. The detailed mathematical expressions for α_1^{+}, α_2^{+}, α_3^{+}, α_4^{+}, α_5^{+}, and α_6^{+} are given in Appendix. K_{2d}^{+} and K_{2q}^{+} represent the direct relationship between the *d*- and *q*-components of $\boldsymbol{I}_{2dq}^{+}$ and $\boldsymbol{U}_{2dq}^{+}$, respectively, and D_{2d}^{+} and D_{2q}^{+} the cross coupling between the PW and the CW.

In the steady state, the PW flux linkage can be regarded as a constant, and thus, the 1st equation of (9) can be simplified as

$$\boldsymbol{U}_{1dq}^{+}=R_1\boldsymbol{I}_{1dq}^{+}+j\omega_2^{+}\boldsymbol{\Psi}_{1dq}^{+}. \quad (24)$$

By splitting (24) and the 1st equation of (9) into the *d*- and *q*-components, the following expressions can be obtained

$$u_{1d}^{+}=R_1 i_{1d}^{+}-\omega_2\psi_{1q}^{+} \quad (25)$$

$$u_{1q}^{+}=R_1 i_{1q}^{+}+\omega_2\psi_{1d}^{+} \quad (26)$$

$$\psi_{1d}^{+}=L_1 i_{1d}^{+}+L_{1r}i_{rd}^{+} \quad (27)$$

$$\psi_{1q}^{+}=L_1 i_{1q}^{+}+L_{1r}i_{rq}^{+}. \quad (28)$$

By combining (16), (17), and (25)-(28), if $i_{2q}^{+}=0$ and $i_{2d}^{+}=I_2^{+}$, u_{1d}^{+} and u_{1q}^{+} can be expressed as

$$u_{1d}^{+}=R_1 i_{1d}^{+}+\frac{\omega_2^{+}(L_{1r}^2-L_1L_r)}{L_r}i_{1q}^{+} \quad (29)$$

$$u_{1q}^{+}=-\frac{\omega_2^{+}(L_{1r}^2-L_1L_r)}{L_r}i_{1d}^{+}+R_1 i_{1q}^{+}-\frac{\omega_2^{+}L_{1r}L_{2r}}{L_r}I_2^{+}. \quad (30)$$

The amplitude of the positive-sequence PW voltage can be expressed as

$$U_1^{+}=\sqrt{(u_{1d}^{+})^2+(u_{1q}^{+})^2}=\left\{\left(\omega_2^{+}\frac{L_{1r}L_{2r}}{L_r}\right)^2(I_2^{+})^2+\left[(i_{1d}^{+})^2+(i_{1q}^{+})^2\right]\left[R_1^2+\left(\omega_2^{+}L_1-\frac{\omega_2^{+}L_{1r}^2}{L_r}\right)^2\right]-\frac{2\omega_2^{+}L_{1r}L_{2r}}{L_r}\left[\left(\omega_2^{+}L_1-\frac{\omega_2^{+}L_{1r}^2}{L_r}\right)i_{1d}^{+}+R_1 i_{1q}^{+}\right]I_2^{+}\right\}^{1/2}. \quad (31)$$

For a small variation in the control variable ΔI_2^{+}, (31) can be approximated by its Taylor expansion as

$$U_1^{+}(I_{2S}^{+}+\Delta I_2^{+})=U_1^{+}(I_{2S}^{+})+\Delta I_2^{+}\left.\frac{dU_1^{+}}{dI_2^{+}}\right|_{I_2^{+}=I_{2S}^{+}} \quad (32)$$

where subscript *S* indicates the steady-state value.

From (32), the relationship between the amplitude increments of the positive-sequence PW voltage and the positive-sequence CW current can be expressed as

$$\Delta U_1^{+}=K_u^{+}\Delta I_2^{+} \quad (33)$$

where

$$K_u^{+}=\omega_2^{+}L_{1r}L_{2r}[\omega_2^{+}L_{1r}L_{2r}I_{2S}^{+}+\omega_2^{+}(L_{1r}^2-L_1L_r)i_{1d}^{+}-R_1L_r i_{1q}^{+}]. \quad (34)$$

I_{2S}^{+} is the amplitude of steady-state positive-sequence CW current.

The amplitude of steady-state positive-sequence PW voltage under I_{2S}^{+} is approximately equal to the amplitude reference of

This article has been accepted for publication in a future issue of this journal, but has not been fully edited. Content may change prior to final publication. Citation information: DOI 10.1109/TIE.2018.2835400, IEEE Transactions on Industrial Electronics

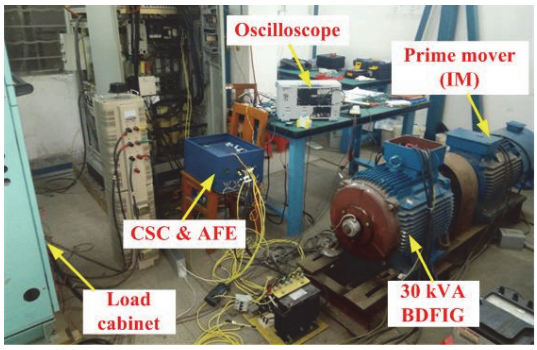

Fig. 4. A photo of the experimental setup.

TABLE I
MAIN PARAMETERS OF PROTOTYPE BDFIG

Parameter	Value
Capacity	30 kVA
Speed range	600 ~1200 rpm
PW and CW pole pairs	1, 3
PW rated voltage and current	380 V, 45 A
CW voltage and current range	0~350 V, 0~50 A
PW, CW, and rotor resistances	0.4034 Ω, 0.2680 Ω, 0.3339 Ω
PW, CW, and rotor self-inductances	0.4749 H, 0.03216 H, 0.2252 H
Mutual inductance between PW and rotor	0.3069 H
Mutual inductance between CW and rotor	0.02584 H
Rotor type	Wound rotor

positive-sequence PW voltage, U_1^{+*}. Therefore, according to (31), I_{2S}^{+} can be derived as

$$I_{2S}^{+}=\frac{(\beta_1^{+}i_{1d}^{+}+R_1 i_{1q}^{+})+[2\beta_1^{+}R_1 i_{1d}^{+}i_{1q}^{+}-R_1^2(i_{1d}^{+})^2-(\beta_1^{+})^2(i_{1q}^{+})^2+U_1^{+*}]^{1/2}}{\beta_2^{+}} \quad (35)$$

where the detailed mathematical expressions for β_1^{+} and β_2^{+} are given in Appendix.

According to (22), (23), and (33)-(35), a cascaded controller for the positive-sequence PW voltage can be designed, as shown in Fig. 3. The controller utilizes a CW current vector controller as the inner loop, and a PW voltage amplitude controller and a frequency controller as the outer loops.

C. Compensation of Negative-Sequence PW Voltage

According to (2), in order to compensate the negative-sequence PW voltage, the CW current frequency should be given by

$$\omega_2^{-}=\omega_r(p_1+p_2)+\omega_1. \quad (36)$$

From (8) and (36), the relationship between ω_2^{+} and ω_2^{-} can be obtained by

$$\omega_2^{-}=\omega_2^{+}+2\omega_1. \quad (37)$$

As it can be seen from (37), the difference between the frequencies of the CW fundamental current and compensation current is twice the PW frequency.

Based on the CW current vector orientation, the angular speed of the *dq* rotation reference frame ω_a in the dynamic vector model should be set as ω_2^{-}. Equation (5) can then be rewritten as

$$\begin{cases} \boldsymbol{U}_{1dq}^{-}=R_1\boldsymbol{I}_{1dq}^{-}+s\boldsymbol{\Psi}_{1dq}^{-}+j\omega_2^{-}\boldsymbol{\Psi}_{1dq}^{-} \\ \boldsymbol{\Psi}_{1dq}^{-}=L_1\boldsymbol{I}_{1dq}^{-}+L_{1r}\boldsymbol{I}_{rdq}^{-} \\ \boldsymbol{U}_{2dq}^{-}=R_2\boldsymbol{I}_{2dq}^{-}+s\boldsymbol{\Psi}_{2dq}^{-}+j[\omega_2^{-}-(p_1+p_2)\omega_r]\boldsymbol{\Psi}_{2dq}^{-} \\ \boldsymbol{\Psi}_{2dq}^{-}=L_2\boldsymbol{I}_{2dq}^{-}+L_{2r}\boldsymbol{I}_{rdq}^{-} \\ \boldsymbol{U}_{rdq}^{-}=R_r\boldsymbol{I}_{rdq}^{-}+s\boldsymbol{\Psi}_{rdq}^{-}+j(\omega_2^{-}-p_1\omega_r)\boldsymbol{\Psi}_{rdq}^{-} \\ \boldsymbol{\Psi}_{rdq}^{-}=L_r\boldsymbol{I}_{rdq}^{-}+L_{1r}\boldsymbol{I}_{1dq}^{-}+L_{2r}\boldsymbol{I}_{2dq}^{-} \end{cases}. \quad (38)$$

Employing a similar method of deriving (22) and (23), one can obtain the following relationships

$$u_{2d}^{-}=K_{2d}^{-}i_{2d}^{-}+D_{2d}^{-} \quad (39)$$

$$u_{2q}^{-}=K_{2q}^{-}i_{2q}^{-}+D_{2q}^{-} \quad (40)$$

where $K_{2d}^{-}=K_{2q}^{-}=R_2+\sigma_2 L_2 s$, $D_{2d}^{-}=\alpha_1^{-}i_{2q}^{-}+\alpha_2^{-}i_{1d}^{-}+\alpha_3^{-}i_{1q}^{-}$, and $D_{2q}^{-}=\alpha_4^{-}i_{2d}^{-}+\alpha_5^{-}i_{1d}^{-}+\alpha_6^{-}i_{1q}^{-}$. The detailed expressions of α_1^{-}, α_2^{-}, α_3^{-}, α_4^{-}, α_5^{-}, and α_6^{-} are given in Appendix.

Similar to (33), the relationship between the amplitude increments of the negative-sequence PW voltage and the negative-sequence CW current can be derived as

$$\Delta U_1^{-}=K_u^{-}\Delta I_2^{-} \quad (41)$$

where

$$K_u^{-}=\omega_2^{-}L_{1r}L_{2r}[\omega_2^{-}L_{1r}L_{2r}I_{2S}^{-}+\omega_2^{-}(L_{1r}^2-L_1L_r)i_{1d}^{-}-R_1L_r i_{1q}^{-}]. \quad (42)$$

Similar to (35), the amplitude of steady-state negative-sequence CW current, I_{2S}^{-}, can be expressed as

$$I_{2S}^{-}=\frac{(\beta_1^{-}i_{1d}^{-}+R_1 i_{1q}^{-})+[2\beta_1^{-}R_1 i_{1d}^{-}i_{1q}^{-}-R_1^2(i_{1d}^{-})^2-(\beta_1^{-})^2(i_{1q}^{-})^2+U_1^{-*}]^{1/2}}{\beta_2^{-}} \quad (43)$$

where the detailed expressions of β_1^{-} and β_2^{-} can be found in Appendix. According to (39)-(43), the negative-sequence PW voltage compensator can be developed, as shown in Fig. 3.

V. EXPERIMENTAL RESULTS

A. Experimental Setup

An experimental setup is shown in Fig. 4. The experiments are performed on a prototype BDFIG, whose detailed parameters are listed in Table I. In this experimental setup, a 37 kW three-phase induction motor driven by a Siemens MM430 inverter is mechanically coupled to the BDFIG and used as the prime mover. The CW is supplied by the control side converter connected with a commercial active front end through dc bus capacitors.

B. Performance Test of Proposed RSO

In this part, an experiment is carried out to test the performance of the proposed RSO when the rotor speed and load vary. During the experiment, the standalone BDFIG system is controlled without compensation of the negative-sequence PW voltage. Since these experimental results are just used to validate whether the RSO can estimate the rotor speed with accuracy similar to that from an encoder under unbalanced load conditions, the observed results are not fed back to the controller.

The initial load is an unbalanced three-phase resistive load with resistances of 12 Ω, 12 Ω, and 6 Ω in phases *a*, *b*, and *c*, respectively. The rotor speed of the BDFIG increases from 550

This article has been accepted for publication in a future issue of this journal, but has not been fully edited. Content may change prior to final publication. Citation information: DOI 10.1109/TIE.2018.2835400, IEEE Transactions on Industrial Electronics

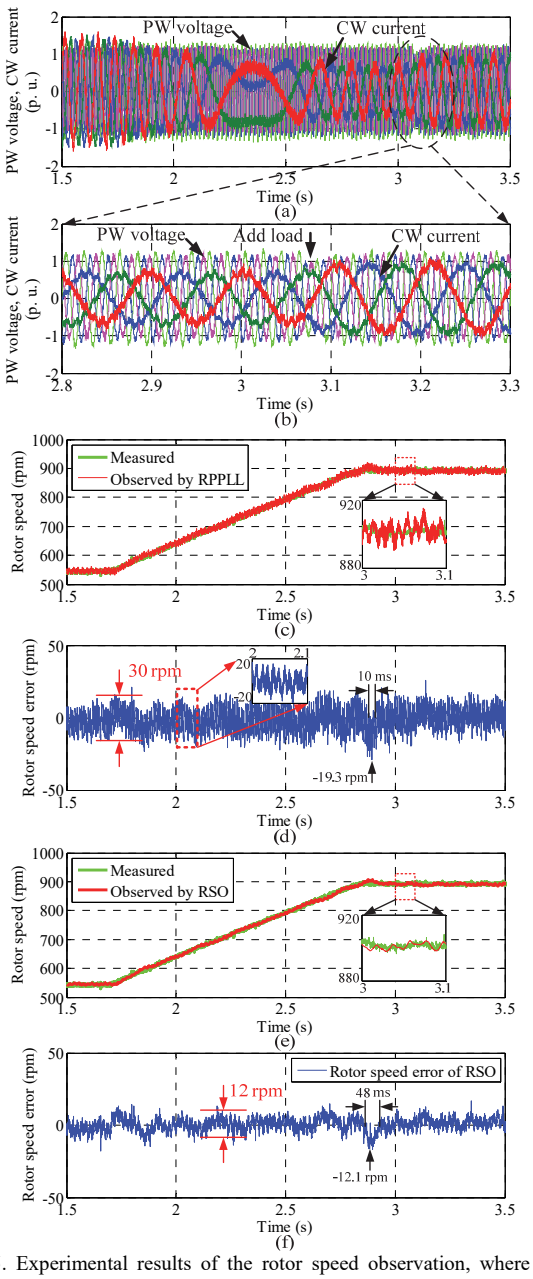

Fig. 5. Experimental results of the rotor speed observation, where (a) PW voltage (1 p. u. = 500 V) and CW current (1 p. u. = 50 A), (b) Detailed view of (a), (c) Rotor speed observed by the basic RSO and measured rotor speed, (d) Error of the rotor speed observed by the basic RSO, (e) Rotor speed observed by the improved RSO and measured rotor speed, and (f) Error of the rotor speed observed by the improved RSO.

rpm to 900 rpm with a rate of 300 rpm per second from 1.7 s to 2.9 s, and then, another unbalanced three-phase resistive load with resistances of 20 Ω, 20 Ω, and 30 Ω in phases *a*, *b*, and *c* is added to the system at 3.08 s.

Fig. 5(a) presents the PW voltage and CW current during the whole process. Fig. 5(b) shows the details of the PW voltage and CW current at around 3.08 s, when the second unbalanced load is applied. From Figs. 5(a) and (b), it can be seen that the PW voltage is unbalanced and the CW current contains abundant harmonics caused by the unbalanced loads. As shown in Figs. 5(d) and (f), at the end of the rotor speed increase, the error of rotor speed observed by the basic RSO reaches -19.3

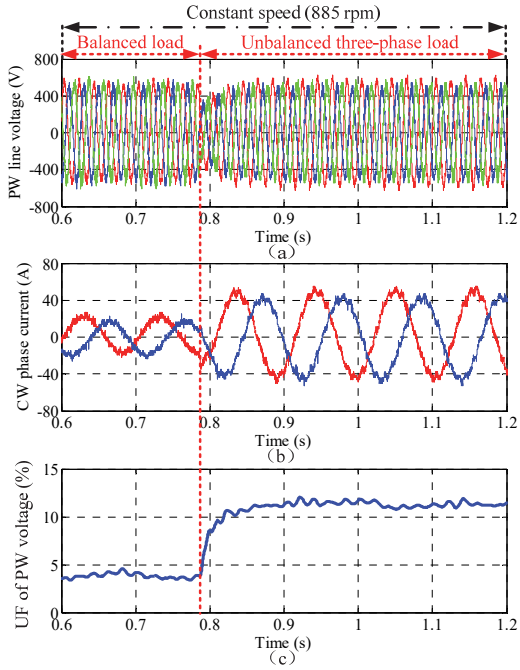

Fig. 6. Experimental results under an unbalanced three-phase load without compensation of the negative-sequence PW voltage, where (a) PW line voltage, (b) CW phase current, and (c) UF of PW voltage.

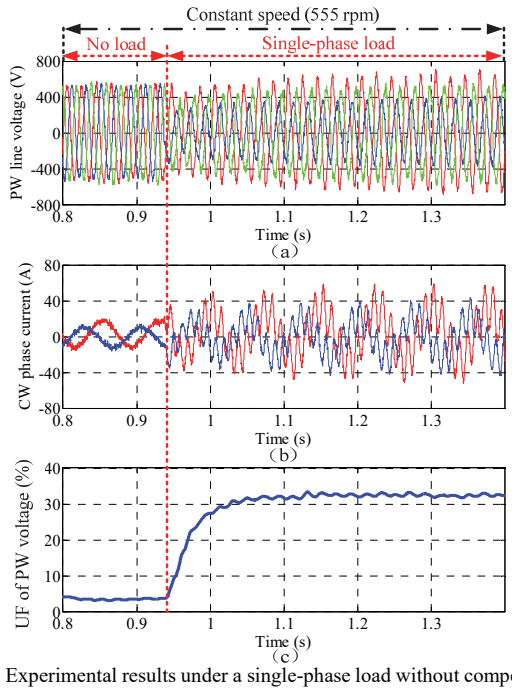

Fig. 7. Experimental results under a single-phase load without compensation of the negative-sequence PW voltage, where (a) PW line voltage, (b) CW phase current, and (c) UF of PW voltage.

rpm with a settling time of 16 ms, and that observed by the improved RSO is reduced to -12.1 rpm with a settling time of 48 ms. Besides, the rotor speed observed by the basic RSO includes a ripple of frequency 100 Hz and peak-to-peak value 30 rpm, as shown in Figs. 5(c) and (d). The ripple of the observed rotor speed can be significantly reduced to about 12 rpm by the improved RSO, as shown in Figs. 5(e) and (f). Therefore, during the rapid rotor speed change, although the improved RSO has a slightly poorer dynamic performance than

This article has been accepted for publication in a future issue of this journal, but has not been fully edited. Content may change prior to final publication. Citation information: DOI 10.1109/TIE.2018.2835400, IEEE Transactions on Industrial Electronics

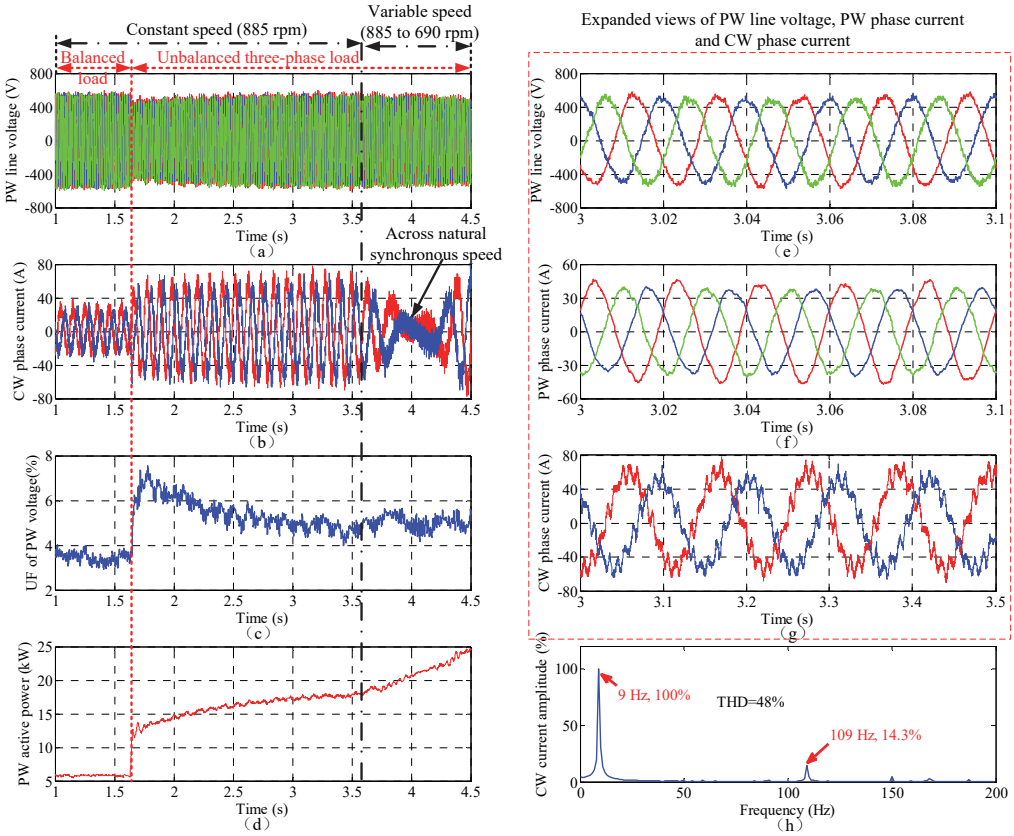

Fig. 8. Experimental results under an unbalanced three-phase load with the compensation of the negative-sequence PW voltage, where (a) PW line voltage, (b) CW phase current, (c) UF of PW voltage, (d) PW active power, (e) Expanded view of (a), (f) PW phase current, (g) Expanded view of (b), and (h) Harmonic spectrum and THD of the CW current as shown in (g).

the basic one, it is with a much smaller steady state error, which is very important for the control of standalone BDFIG. When another unbalanced three-phase load is added at 3.08 s, the error of the rotor speed observed by the improved RSO is almost zero under the 17% transient drop of the PW voltage amplitude and the 30% increase of the CW current amplitude as shown in Figs. 5(a) and (b), which demonstrates good dynamic performance of the improved RSO during the load variation.

C. Results without Compensation of Negative-Sequence PW Voltage

To clearly illustrate the performance of the proposed control scheme, the system characteristics under unbalanced three-phase load and single-phase load without compensation of the negative-sequence PW voltage are presented in Experiments 1 and 2. The single-phase load is a special case of the unbalanced three-phase load, which usually causes more serious unbalance of the output voltage. In all the experiments, the amplitude and frequency references of the PW line voltage are set as 380 V and 50 Hz, respectively. The experimental results are presented in Figs. 6 and 7.

Experiment 1: The rotor speed of the BDFIG is kept constant at 885 rpm. The initial load is a balanced three-phase resistive load with resistance of 25 Ω in each phase, and an unbalanced three-phase resistive load with resistances of 12 Ω, 12 Ω, and 6 Ω in phases *a*, *b*, and *c* is added to the system at 0.78 s. As shown in Figs. 6(a) and (b), the unbalanced load causes the PW voltage unbalanced with an unbalance factor (UF) of 12%, and distorts the CW current through the coupling of the BDFIG rotor, as shown in Fig. 6(c).

Experiment 2: The rotor speed is kept constant at 555 rpm. The BDFIG is initially operated at no load, and at 0.94 s, a single-phase load with resistance of 12 Ω is connected between phases *a* and *b* of the PW, which causes the UF of PW voltage increase dramatically to 32% and the distortion of CW current is much severer than that in Experiment 1, as shown in Fig. 7.

D. Results with Compensation of Negative-Sequence PW Voltage

With the compensation of negative-sequence PW voltage, Experiments 3 and 4 are carried out to verify the performance of the proposed control scheme under variable loads and rotor speeds when supplying unbalanced three-phase and single-phase loads. The experimental results are shown in Figs. 8 and 9.

Experiment 3: The rotor speed is initially 885 rpm, and from 3.63 s to 4.50 s, it drops to 690 rpm at a rate of 225 rpm per second. The load change occurs at 1.65 s, and the balanced and unbalanced three-phase loads used in this experiment are the same as those in Experiment 1. The overall PW line voltage waveforms are presented in Fig. 8(a). Fig. 8(b) illustrates the overall CW phase current waveforms, in which a smooth change of the CW current phase sequence across the natural synchronous speed (750 rpm) of the BDFIG can be seen at about 4 s. As shown in Fig. 8(c), the UF of the PW voltage under the unbalanced load can be reduced to about 5%, which is

This article has been accepted for publication in a future issue of this journal, but has not been fully edited. Content may change prior to final publication. Citation information: DOI 10.1109/TIE.2018.2835400, IEEE Transactions on Industrial Electronics

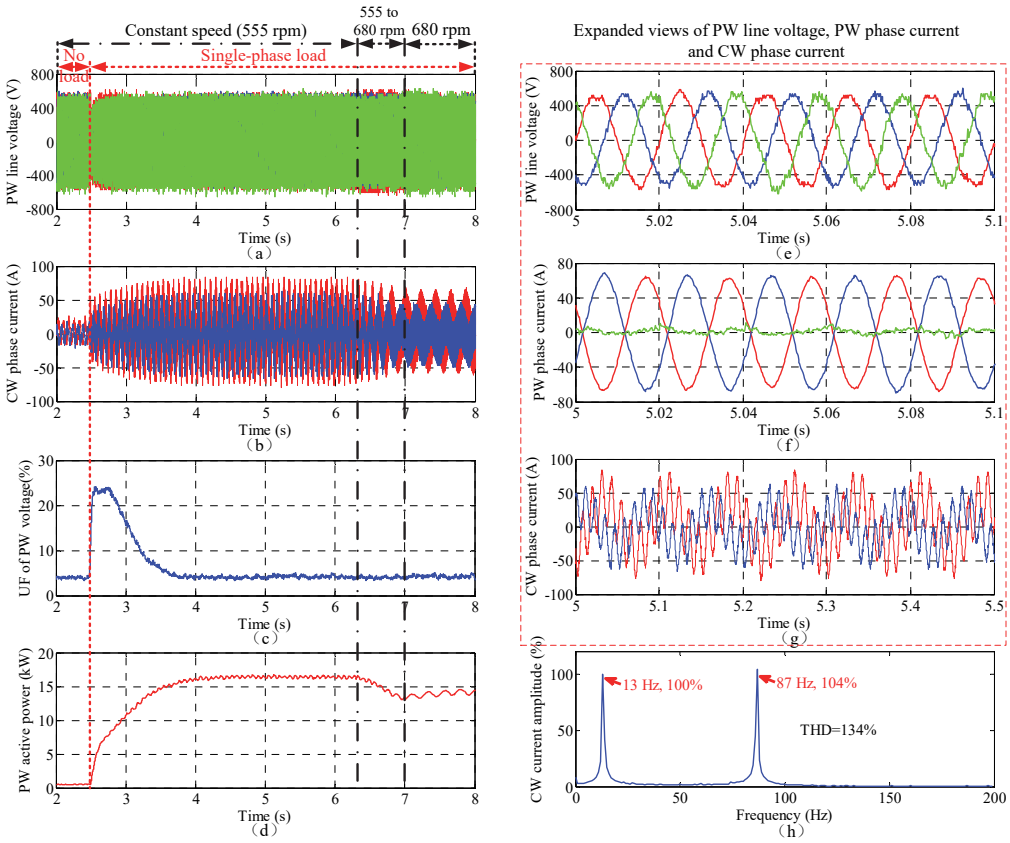

Fig. 9. Experimental results under a single-phase load with the compensation of the negative-sequence PW voltage, where (a) PW line voltage, (b) CW phase current, (c) UF of PW voltage, (d) PW active power, (e) Expanded view of (a), (f) PW phase current, (g) Expanded view of (b), and (h) Harmonic spectrum and THD of the CW current as shown in (g).

much less than that without compensation of the negative-sequence PW voltage as shown in Fig. 6(c). During the rapid rotor speed variation between 3.63 s and 4.5 s, the UF of PW voltage is not significantly changed. The PW active power during the whole process is shown in Fig. 8(d). The initial PW active power under the balanced load is 5.8 kW. After the unbalanced three-phase load is applied, the PW active power rises rapidly to 12.3 kW. As the PW voltage converges to its reference value, the PW active power gradually increases to 17.5 kW. During the rotor speed drop, the PW active power rises to 24.1 kW, which is consistent with the relationship between the PW active power and rotor speed as shown in (4).

Figs. 9(e), (f) and (g) show the details of the PW line voltage, PW phase current and CW phase current after the compensation, respectively. Although the negative-sequence PW voltage can be successfully compensated, the PW current becomes unbalanced, as shown in Fig. 8(f), due to the effects of the unbalanced three-phase load. As shown in Fig. 8(g), in order to compensate the negative-sequence PW voltage, a harmonic component is injected into the CW current. Fig. 8(h) presents the harmonic spectrum and total harmonic distortion (THD) of the CW current as shown in Fig. 8(g). The fundamental frequency of the CW current is 9 Hz, which is determined by the rotor speed according to (2). The harmonic has the frequency of 109 Hz, which coincides with (37), and the THD of the CW current reaches 48%.

Experiment 4: The standalone BDFIG is initially operated under no load, and at 2.48 s, the same single-phase load as that in Experiment 2 is connected to the system. Before 6.3 s, the rotor speed is 555 rpm, and then it rises to 680 rpm with a rate of 180 rpm per second. After 7 s, the rotor speed is kept constant at 680 rpm. The overall PW line voltage and CW phase current waveforms are illustrated in Figs. 9(a) and (b), respectively. Fig. 9(c) presents the UF of PW voltage under the single-phase load. When the single-phase load is connected to the system, the UF of PW voltage is up to about 24%, and then reduced to 4% within 1.2 s. During the rotor speed variation, the UF of PW voltage is almost constant. After the single-phase load is connected to the system, the PW active power gradually increases to about 16.2 kW as the PW voltage converges to its reference value. When the rotor speed increases to 680 rpm, the PW active power reduces to 13.2 kW, which can be explained by the relationship between the PW active power and rotor speed as shown in (4).

The expanded views of the PW line voltage, PW phase current and CW phase current after the compensation are shown in Figs. 9(e), (f) and (g), respectively. Although the negative-sequence PW voltage is almost fully compensated, due to the effect of single-phase load, two-phase PW currents are in the opposite directions, and the third phase current is nearly zero, as shown in Fig. 9(f). Since a single-phase load is a more severely unbalanced load, more harmonics need to be injected into the CW current in order to compensate the negative-sequence PW voltage, as shown in Fig. 9(g). The harmonic spectrum and THD of the CW current between 5 s and 5.5 s are shown in Fig. 9(h). The CW current contains a

This article has been accepted for publication in a future issue of this journal, but has not been fully edited. Content may change prior to final publication. Citation information: DOI 10.1109/TIE.2018.2835400, IEEE Transactions on Industrial Electronics

fundamental component with the frequency of 13 Hz, and a significant harmonic component with the frequency of 87 Hz. Because the BDFIG operates at a sub-synchronous speed of 555 rpm, the fundamental frequency of the CW current is -13 Hz (the negative frequency indicating that the phase sequence of the CW current is opposite to that of the CW current at a super-synchronous speed), which shows that the difference between the fundamental and harmonic frequencies of the CW current still matches (37). The amplitude of the CW current harmonic component is greater than that of the fundamental, which results in the THD of CW current being up to 134%.

VI. Conclusion

This paper presents a RSO and a sensorless control scheme for the standalone BDFIG feeding unbalanced loads in a ship shaft power generation system. The positive- and negative-sequence components of the unbalanced PW voltage caused by the unbalanced loads are regulated separately in the proposed control scheme. A RSO is designed for the unbalanced operation of the standalone BDFIG, which is independent to machine parameters except the number of pole pairs. Based on the proposed RSO, a sensorless control scheme for the standalone BDFIG feeding unbalanced loads is presented. Comprehensive experiments have been carried out on a BDFIG prototype with and without compensation of the negative-sequence PW voltage. It is confirmed by the experimental results that the proposed control scheme can significantly reduce the unbalance of the output voltage and thus improve the output voltage quality under unbalanced loads. Furthermore, the harmonic elimination method of standalone BDFIG ship shaft power generation systems with nonlinear loads would be another important work in the future.

Appendix

$$\alpha_1^+ = \frac{\omega_1(\omega_1 - p_2\omega_r)(L_r^2 L_2 + L_{2r}^2 L_r) - L_{2r}^2 R_r s}{L_r^2(\omega_1 - p_2\omega_r)} \tag{44}$$

$$\alpha_2^+ = -\frac{L_{1r}L_{2r}s}{L_r},\ \alpha_3^+ = -\frac{L_{1r}L_{2r}[R_r s + L_r\omega_1(\omega_1 - p_2\omega_r)]}{L_r^2(\omega_1 - p_2\omega_r)} \tag{45}$$

$$\alpha_4^+ = -\frac{\sigma_2 L_2 L_r \omega_1}{L_1},\ \alpha_5^+ = \frac{\omega_1 L_{1r} L_{2r}}{L_r} \tag{46}$$

$$\alpha_6^+ = \frac{L_{1r}L_{2r}\left[\omega_1 R_r - L_r(\omega_1 - p_2\omega_r)s\right]}{L_r^2(\omega_1 - p_2\omega_r)} \tag{47}$$

$$\beta_1^+ = \omega_2^+ L_1 - \omega_2^+ L_{1r}^2 / L_r,\ \beta_2^+ = \omega_2^+ L_{1r} L_{2r} / L_r \tag{48}$$

$$\alpha_1^- = -\frac{\omega_1(\omega_1 + p_2\omega_r)(L_r^2 L_2 + L_{2r}^2 L_r) + L_{2r}^2 R_r s}{L_r^2(\omega_1 + p_2\omega_r)} \tag{49}$$

$$\alpha_2^- = -\frac{L_{1r}L_{2r}s}{L_r},\ \alpha_3^- = \frac{L_{1r}L_{2r}[R_r s + L_r\omega_1(\omega_1 + p_2\omega_r)]}{L_r^2(\omega_1 + p_2\omega_r)} \tag{50}$$

$$\alpha_4^- = -\frac{\sigma_2 L_2 L_r \omega_1}{L_1},\ \alpha_5^- = -\frac{\omega_1 L_{1r} L_{2r}}{L_r} \tag{51}$$

$$\alpha_6^- = -\frac{L_{1r}L_{2r}\left[\omega_1 R_r + L_r(\omega_1 + p_2\omega_r)s\right]}{L_r^2(\omega_1 + p_2\omega_r)} \tag{52}$$

$$\beta_1^- = \omega_2^- L_1 - \omega_2^- L_{1r}^2 / L_r,\ \beta_2^- = \omega_2^- L_{1r} L_{2r} / L_r \tag{53}$$

References

[1] S. Williamson, A. C. Ferreira, and A. K. Wallace, "Generalised theory of the brushless doubly-fed machine. Part 1: analysis," *IEE Proc.-Elect. Power Appl.*, vol. 144, no. 2, pp. 111-122, Mar. 1997.

[2] M. Ruviaro, F. Rüncos, N. Sadowski, and I. M. Borges, "Analysis and test results of a brushless doubly fed induction machine with rotary transformer," *IEEE Trans. Ind. Electron.*, vol. 59, no. 6, pp. 2670-2677, Jun. 2012.

[3] R. A. McMahon, P. C. Roberts, X. Wang, and P. J. Tavner, "Performance of BDFM as generator and motor," *IEE Proc.-Elect. Power Appl.*, vol. 153, no. 2, pp. 289-299, Mar. 2006.

[4] Y. Liu, W. Ai, B. Chen, K. Chen, and G. Luo, "Control design of the brushless doubly-fed machine for stand-alone VSCF ship shaft generator systems," *Journal of Power Electron.*, vol. 16, no. 1, pp. 259-267, Jan. 2016.

[5] S. Shao, E. Abdi, F. Barati, and R. A. McMahon, "Stator-flux-oriented vector control for brushless doubly-fed induction generator," *IEEE Trans. Ind. Electron.*, vol. 56, no. 10, pp. 4220-4228, Oct. 2009.

[6] S. Shao, T. Long, E. Abdi, and R. A. McMahon, "Dynamic control of the brushless doubly fed induction generator under unbalanced operation," *IEEE Trans. Ind. Electron.*, vol. 60, no. 6, pp. 2465-2476, June 2013.

[7] J. Chen, W. Zhang, B. Chen, and Y. Ma, "Improved vector control of brushless doubly fed induction generator under unbalanced grid conditions for offshore wind power generation," *IEEE Trans. Energy Convers.*, vol. 31, no. 1, pp. 293-302, Mar. 2016.

[8] X. Wei, M. Cheng, W. Wang, P. Han, R. Luo, "Direct voltage control of dual-stator brushless doubly fed induction generator for stand-alone wind energy conversion systems," *IEEE Trans. Magnetics*, vol. 52, no. 7, Jul. 2016.

[9] X. Wang, H. Lin, Z. Wang, "Transient control of reactive current for line-side converter of brushless doubly fed induction generator in stand-alone operation," *IEEE Trans. Power Electron.*, vol. 32, no. 10, pp. 8193-8203, Oct. 2017.

[10] Y. Liu, W. Ai, B. Chen, and K. Chen, "Control design and experimental verification of the brushless doubly-fed machine for stand-alone power generation applications," *IET Elect. Power Appl.*, vol. 10, no. 1, pp. 25-35, Jan. 2016.

[11] Y. Liu, W. Xu, G. Zhi, J. Zhang, "Performance analysis of the stand-alone brushless doubly-fed induction generator by using a new T-type steady-state model," *Journal of Power Electron.*, vol. 17, no. 4, pp. 1027-1036, Jul. 2017.

[12] T. Long, S. Shao, P. Malliband, E. Abdi, and R. A. McMahon, "Crowbarless fault ride-through of the brushless doubly fed induction generator in a wind turbine under symmetrical voltage dips," *IEEE Trans. Ind. Electron.*, vol. 60, no. 7, pp. 2833-2840, Jul. 2013.

[13] F. Barati, R. McMahon, S. Shao, E. Abdi, and H. Oraee, "Generalized vector control for brushless doubly fed machines with nested-loop rotor," *IEEE Trans. Ind. Electron.*, vol. 60, no. 6, pp. 2477-2485, Jun. 2013.

[14] S. Shao, E. Abdi, and R. McMahon, "Low-cost variable speed drive based on a brushless doubly-fed motor and a fractional unidirectional converter," *IEEE Trans. Ind. Electron.*, vol. 59, no. 1, pp. 317-325, Jan. 2012.

[15] A. Zhang, X. Wang, W. Jia, and Y. Ma, "Indirect stator-quantities control for the brushless doubly fed induction machine," *IEEE Trans. Power Electron.*, vol. 29, no. 3, pp. 1392-1401, Mar. 2014.

[16] I. Sarasola, J. Poza, M. A. Rodriguez, and G. Abad, "Direct torque control design and experimental evaluation for the brushless doubly fed machine," *Energy Conversion and Management*, vol. 52, no. 2, pp. 1226-1234, Feb. 2011.

[17] L. Sun, Y. Chen, J. Su, D. Zhang, L. Peng, Y. Kang, " Decoupling network design for inner current loops of stand-alone brushless doubly fed induction generation power system," *IEEE Trans. Power Electron.*, in press.

[18] S. Ademi, M. G. Jovanović, "A novel sensorless speed controller design for doubly-fed reluctance wind turbine generators," *Energy Conversion and Management*, vol. 120, pp. 229-237, 2016.

[19] S. Ademi, M. G. Jovanović, H. Chaal, W. Cao, "A new sensorless speed control scheme for doubly fed reluctance generators," *IEEE Trans. Energy Convers.*, vol. 31, no. 3, pp. 993-1001, Mar. 2016.

[20] J. Poza, E. Oyarbide, D. Roye, and M. Rodriguez, "Unified reference frame dq model of the brushless doubly fed machine," *IEE Proc.-Elect. Power Appl.*, vol. 153, no. 5, pp. 726-734, Sep. 2006.

[21] S.-K. Chung, "Phase-locked loop for grid-connected three-phase power conversion systems," *IEE Proc.-Elect. Power Appl.*, vol. 147, no. 3, pp.213–219, May 2000.

[22] Y. Liu, W. Xu, T. Long, and F. Blaabjerg, "A new rotor speed observer for stand-alone brushless doubly-fed induction generators," *2017 IEEE Energy Conversion Congress and Exposition (ECCE)*, Cincinnati, OH, USA, Oct. 2017, pp. 5086-5092.

[23] S. Golestan, M. Monfared, F. D. Freijedo, "Design-oriented study of advanced synchronous reference frame phase-locked loops," *IEEE Trans. Power Electron.*, vol. 28, no. 2, pp. 765-778, Feb. 2013.

Yi Liu (M'14) received his B.E. and M.E. degrees in Automation and Control Engineering from the Wuhan University of Science and Technology, Wuhan, China, in 2004 and 2007, respectively; and his Ph.D. degree in Mechatronic Engineering from the Huazhong University of Science and Technology, Wuhan, China, in 2016.

From 2007 to 2011, he was a Lecturer at the Wuhan University of Science and Technology. From March 2016 to June 2016, he was a Senior R & D Engineer at the Fourth Academy of China Aerospace Science and Industry Group, Wuhan, China. In July 2016, he became a Postdoctoral Research Fellow at the State Key Laboratory of Advanced Electromagnetic Engineering and Technology, Huazhong University of Science and Technology.

His current research interests include AC electrical machine control and inverter systems.

Wei Xu (M'09-SM'13) received the double B.E. and M.E. degrees from Tianjin University, Tianjin, China, in 2002 and 2005, and the Ph.D. from the Institute of Electrical Engineering, Chinese Academy of Sciences, in 2008, respectively, all in electrical engineering.

From 2008 to 2012, he held several academic positions in both Australian and Japanese universities and companies. Since 2013, he has been full professor with the State Key Laboratory of Advanced Electromagnetic Engineering and Technology, Huazhong University of Science and Technology, China.

His research topics mainly cover design and control of linear/rotary machines.

Jianguo Zhu (S'93–M'96–SM'03) received the B.E. degree in 1982 from Jiangsu Institute of Technology, Jiangsu, China, the M.E. degree in 1987 from Shanghai University of Technology, Shanghai, China, and the Ph.D. degree in 1995 from the University of Technology Sydney (UTS), Sydney, Australia, all in electrical engineering.

He was appointed a lecturer at UTS in 1994 and promoted to full professor in 2004 and Distinguished Professor of Electrical Engineering in 2017. In 2018, he joined the University of Sydney, Australia, as a full professor and Head for School of Electrical and Information Engineering.

His research interests include computational electromagnetics, measurement and modelling of magnetic properties of materials, electrical machines and drives, power electronics, renewable energy systems and smart micro grids.

Frede Blaabjerg (S'86–M'88–SM'97–F'03) was with ABB-Scandia, Randers, Denmark, from 1987 to 1988. From 1988 to 1992, he got the PhD degree in Electrical Engineering at Aalborg University in 1995. He became an Assistant Professor in 1992, an Associate Professor in 1996, and a Full Professor of power electronics and drives in 1998. From 2017 he became a Villum Investigator.

His current research interests include power electronics and its applications such as in wind turbines, PV systems, reliability, harmonics and adjustable speed drives. He has published more than 500 journal papers in the fields of power electronics and its applications. He is the co-author of two monographs and editor of 7 books in power electronics and its applications.

He has received 24 IEEE Prize Paper Awards, the IEEE PELS Distinguished Service Award in 2009, the EPE-PEMC Council Award in 2010, the IEEE William E. Newell Power Electronics Award 2014 and the Villum Kann Rasmussen Research Award 2014. He was the Editor-in-Chief of the IEEE TRANSACTIONS ON POWER ELECTRONICS from 2006 to 2012. He has been Distinguished Lecturer for the IEEE Power Electronics Society from 2005 to 2007 and for the IEEE Industry Applications Society from 2010 to 2011 as well as 2017 to 2018. In 2018 he is President Elect of IEEE Power Electronics Society.

He is nominated in 2014, 2015, 2016 and 2017 by Thomson Reuters to be between the most 250 cited researchers in Engineering in the world. In 2017 he became Honoris Causa at University Politehnica Timisoara (UPT), Romania.